# Electrically Small Antenna with a Significantly Enhanced Gain-Bandwidth Product

Yaqing Yu, *Student Member, IEEE*, Ming-Chun Tang, *Senior Member, IEEE*, Da Yi, *Member, IEEE*, Dingmou Hong, *Student Member, IEEE*, Ting Shi, *Member, IEEE*, and Richard W. Ziolkowski, *Life Fellow, IEEE*

***Abstract*—Extremely electrically small antennas (XESAs) exhibit low gain performance, which seriously limits their applications in space-constrained wireless platforms. We report an active transmitting XESA whose gain-bandwidth product (GBWP) exceeds the passive Bode-Fano upper-bound. It is realized by incorporating a highly efficient, electrically small near-field resonant parasitic (NFRP) antenna into the feedback loop of an operational amplifier (OpAmp). Rather than a cascaded configuration, the innovative structural embedding of the NFRP antenna directly with the OpAmp circuit significantly increases its effective gain without consuming any additional real estate. The operating mechanisms of the integrated system are explained with an equivalent circuit model. An optimized prototype was fabricated, assembled and tested. The electrical size of its radiating element is extremely small with *ka* = 0.15 at 414 MHz, i.e., a ≈ λ/42. The measured results of this active XESA, in good agreement with their simulated values, demonstrate that its effective gain can be dynamically tuned within a 6.01 dB range. The measured maximum effective gain and, hence, the effective isotropic radiated power (*EIRP*) witnesses a 9.152 dB (8.23 times) improvement in comparison to its passive counterpart and its measured GBWP surpasses the corresponding passive Bode-Fano upper bound by approximately 15.2 times.**

***Index Terms*— Active antennas, amplifiers, electrically small antennas (ESAs), feedback, gain, near-field resonant parasitic (NFRP) elements, operational amplifiers (OpAmp).**

## I. Introduction

Electrically small antennas (ESAs) have always been a hot research topic because of their sizes are small in comparison to their operational wavelengths, which makes them useful for a wide variety of wireless applications associated with space-limited platforms [1]-[5]. However, the basic physics associated with their electrically small sizes inherently limit their performance characteristics, e.g., their impedance bandwidths and realized gain values. Those bounds are described by Bode-Fano theory [6], [7] and the Chu-Wheeler-Harrington limits [8]-[11].

In order to significantly extend the operating bandwidth of an ESA while maintaining its radiation performance, active non-Foster circuits have been considered both in external/cascaded impedance matching [12]-[18] and internal/embedded reactance matching [19]-[28] configurations. The non-Foster elements can be tailored to actively match the resistance and reactance values of the antenna to the source in the former and actively match the negative reactance-to-frequency slope arising in the latter over large bandwidths.

On the other hand, many approaches have been taken to improve the maximum realized gain values of ESAs. These include designing Yagi-configurations [29]; introducing superstrates [30], [31] and near-field resonant parasitic (NFRP) elements [32], [33]; and developing Huygens dipole antennas [34]-[37]. While effective, the improvements of their gain values are still limited when the volumes of these passive ESAs are constrained. This is particularly true when their electric sizes are quite small, e.g., $ka < 0.2$ ($a$ being the radius of the smallest sphere enclosing the radiator and $k$ is the free-space wavenumber at the resonance frequency $f_0$). The maximum realized gain of such an ESA is generally quite low, e.g., -15 dBi in [38]. Consequently, it is very challenging to engineer systems with space-constraints to meet the demands of scenarios where large signal attenuation is involved and high-gain transmission becomes necessary. For instance, Internet of Things (IoT) [39] and smart home access [40] wireless devices must operate in the presence of thick reinforced concrete walls, atmospheric conditions and high multipath noise levels.

Active circuits have been employed widely to increase the effective gain of a wireless system. A common method is to directly cascade an active amplifier circuit with a passive antenna to significantly increase its effective gain [41]-[45]. However, the circuits and transmission lines in a cascade configuration significantly increase a system's overall size. As a consequence, the cascade approach is not generally suitable to achieve an overall electrically small design.

An electrically small active radiator with enhanced effective gain is developed in this paper that avoids the cascade configuration. It is facilitated by co-designing and seamlessly combining a NFRP ESA with an operational amplifier (OpAmp) circuit. The NFRP ESA is embedded into the feedback loop of the OpAmp circuit in a systematic manner that does not increase the radius of the minimum enclosing sphere surrounding the original passive ESA. The NFRP element serves two functions. On the one hand, it

Manuscript received on January 30, 2021; revised on October 06, 2021; and accepted on October 28, 2021.

This work was supported in part by the National Natural Science Foundation of China under Contracts 62001065 and 62061006, in part by the Chongqing Natural Science Foundation under Contract cstc2019jcyjjqX0004, and in part by the Australian Research Council under Grant DP160102219. (Corresponding author: *Ming-Chun Tang.*)

Y. Yu, M.-C. Tang, D. Yi, D. Hong and T. Shi are with the Key Laboratory of Dependable Service Computing in Cyber Physical Society Ministry of Education, College of Microelectronics and Communication Engineering, Chongqing University, Chongqing 400044, China (E-mail: tangmingchun@cqu.edu.cn).

R. W. Ziolkowski is with the University of Technology Sydney, Global Big Data Technologies Centre, Ultimo NSW 2007, Australia (E-mail: Richard.Ziolkowski@uts.edu.au).

functions as the main radiator of the ESA system [32], [33]. On the other hand, it serves as a lossy resonator in the negative feedback loop and, hence, facilitates the tunability of the effective gain of the entire ESA system. When compared to its passive counterpart, the active ESA attains a 9.152 dB enhancement of the maximum effective gain while maintaining its *ka* value.

The remaining sections are organized as follows. The basic design principles of the active ESA are described first in Section II. The configuration and design parameters of the active ESA are introduced. Then, the layout of the active OpAmp circuit, the geometry of the passive NFRP antenna and the integration approach are detailed in a step-by-step manner. Next, an equivalent circuit model of the active NFRP ESA is developed and its efficacy is demonstrated. The fabrication, assembly and testing of an optimized active ESA prototype whose size is extremely electrically small with $ka$ = 0.15 are described next in Section III. The measured results of this extremely electrically small antenna (XESA) prototype, in good agreement with their simulated values, demonstrate that it achieved a maximum effective gain of 7.232 dBi and a gain-bandwidth product (*GBWP*) of 0.0513, which surpasses the corresponding passive Bode-Fano upper bound by 15.2 times. Finally, conclusions are drawn in Section IV.

We note that the dielectric and metallic elements were modeled with their known parameters in all of the reported numerical simulations. For instance, all traces were copper with its known material parameters: $\varepsilon_r$ = 1.0, $\mu_r$ = 0.999991 and bulk conductivity $\sigma = 5.8 \times 10^7$ S/m. The copper-clad substrates are all Rogers Duroid™ 5880 whose relative permittivity is 2.2, loss tangent is 0.0009, and copper thickness is 0.017 mm. The co-design of the antenna and OpAmp circuit were performed using the frequency domain ANSYS/ANSOFT high frequency structure simulator (HFSS), version 17.0, and Agilent's Advanced Design System (ADS), 2009. The optimization of the overall system was guided by previous NFRP ESA designs and the developed circuit model of the OpAmp system and relied on numerical parameter studies to determine the fine details.

## II. Design of the Effective Gain Enhanced XESA

The basic cascaded and embedded OpAmp-ESA combinations are represented by the diagrams shown in Fig. 1. The OpAmp circuit in Fig 1(a) illustrates the standard ideal non-inverting negative-feedback design. The combination depicted by Figs. 1(a) and 1(b) represents the conventional approach to design the front-end of a system, i.e., the amplifier and the ESA are designed individually and then cascaded. To address the associated increased size issue, we introduced the innovative design developed herein that is depicted in Fig. 1(c). The ESA is embedded in the feedback loop of the OpAmp circuit. We have developed the unconventional manner shown below in Fig. 2 to combine the two individual components in a co-shared volume.

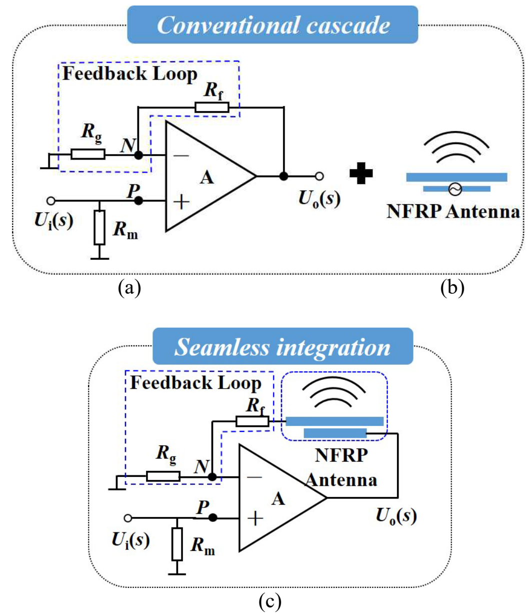

Fig. 1 The evolution of the integrated active NFRP ESA (a) OpAmp circuit. (b) NFRP antenna in series with the OpAmp. (c) NFRP antenna embedded in the negative feedback loop of the OpAmp circuit.

### A. Active ESA configuration

The various components of the combined OpAmp-ESA configuration are shown in Fig. 2. The system consists of an active OpAmp circuit and a modified version of the 2D magnetic EZ ESA introduced in [46] in which the NFRP element is a capacitively loaded loop (CLL) and the driven element is a coax-fed semi-loop antenna. Their compact integration is illustrated in Fig. 2(a). The CLL and semi-loop elements are printed on the same side of a rectangular sheet of the Rogers Duroid™ 5880 material, Sub_1, that is $h_1$ = 0.787 mm thick. The NFRP element is excited by the driven element and is the primary radiator. One end of the driven element and both ends of the NFRP element are connected to the ground plane, which is a copper disk whose thickness $h_2$ = 1.0 mm and radius is 180 mm. As shown in Figs. 2(a) and 2(c), the OpAmp circuit is printed on Sub_2, another sheet of the same Rogers 5880 substrate. Note that the driven element is split and a small gap is present between the two strips shown in pink. The latter are then connected to the positive input and output ports of the OpAmp. The NFRP element thus becomes a part of the feedback loop that is connected to the negative input port of the OpAmp through the green stubs, stub_1 and stub_2, which lie on opposite sides of Sub_1. The optimized design parameters of the system as shown in Fig 2 are listed in Table I.

Table I Optimized Design Parameters of the Active ESA (All Dimensions are in Millimeters)

| | | | | |
|---|---|---|---|---|
| $L_1$ = 13.8 | $L_2$ = 1.91 | $L_3$ = 11.69 | $L_4$ = 4 | $L_5$ = 3 |
| $L_6$ = 6.39 | $L_7$ = 3.46 | $L_8$ = 10 | $L_9$ = 1.89 | $L_{10}$ = 2.78 |
| $L_{11}$ = 10 | $W_1$ = 22.4 | $W_2$ = 2.4 | $W_3$ = 8.4 | $W_4$ = 7.3 |
| $W_5$ = 0.2 | $W_6$ = 20 | $h_1$ = 0.787 | $h_2$ = 1 | $g_1$ = 0.4 |

The active OpAmp circuit is detailed in Fig. 2(c). The OPA855 chip from Texas Instruments (TI) was selected because it has several advantageous features including a large GBWP, a wide bandwidth and low noise characteristics [47].

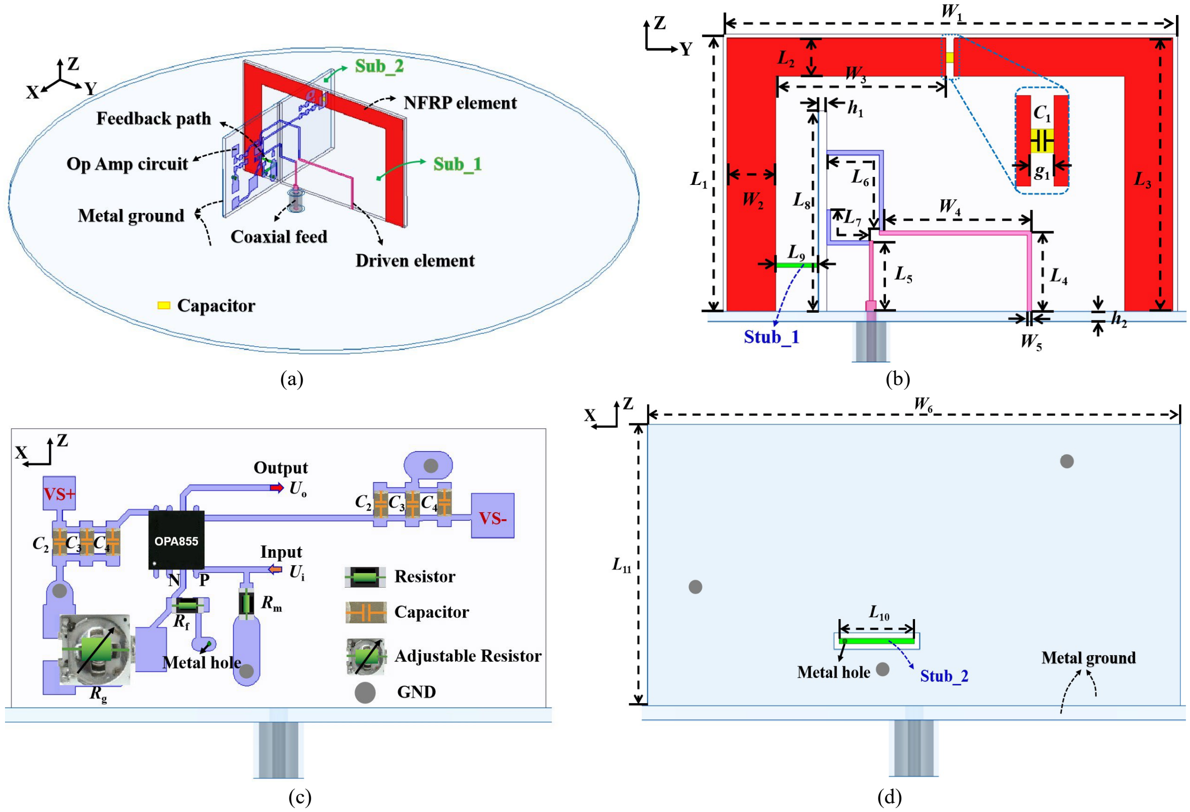


Fig. 2 The proposed active ESA configuration and its design parameters. (a) 3-D isometric view. (b) Front surface of Sub_1. (c) The geometry of the OpAmp circuit on the front surface of Sub_2. (d) Back surface of Sub_2.

The resistor $R_m$ = 50 Ω, which is connected in parallel between the coaxial feed and the positive input port of the OpAmp, is used to match the relatively large input impedance of the OpAmp. The capacitors $C_2$, $C_3$ and $C_4$ in the bias circuits are employed to prevent RF signals from propagating into the DC power source, which supplies the voltages $VS^+$ and $VS^-$ to the OpAmp. Note that the non-inverting operation utilized here is a typical series-voltage negative feedback circuit. The feedback signal $U_o$ is taken from the output port and flows through the NFRP element. It is then divided by the resistors $R_f$ and $R_g$. The feedback voltage on $R_g$ facilitates changing the gain factor of the OpAmp. The element values of the active ESA are detailed in Table II.

TABLE II ELEMENT VALUES OF THE ACTIVE ESA

| | | | |
|---|---|---|---|
| $C_1$ = 5.6 pF | $C_2$ = 0.01 μF | $C_3$ = 0.22 μF | $C_4$ = 2.2 μF |
| $R_m$ = 50 Ω | $R_f$ = 499 Ω | $R_g$ = ~2 kΩ | *NULL* |

The closed-loop amplification factor $A_f$ of the OpAmp circuit is calculated as [48]

$$A_f = 1 + \frac{R_f}{R_g} \tag{1}$$

Since the resistance $R_g$ is adjustable, the magnitude of $A_f$ and, hence, the effective gain value of the active ESA can be adjusted appropriately. This enables the overall system to be energy smart because its energy consumption can be controlled to use only the energy that is needed to meet the different requirements in a complicated wireless environment associated with multiple communication distances and complex signal channels. It is important to emphasize that the so-called "effective gain" (see [49], [50]) will be utilized herein to evaluate the gain performance of the active ESA while the "realized gain" will be used for its passive counterpart.

### *B. Design steps and performance analysis*

The procedure used to design the active ESA was divided into three steps. First, the frequency-dependent performance of the OpAmp circuit is evaluated with a practical prototype. Its design and its fabricated prototype are shown in Fig. 3. This step allows one to determine the tunable range of the transducer power gain in preparation for its application in the active ESA design. According to its datasheet [47], the common-mode input impedance of the OPA855 chip is as high as $R_{c\text{-}in}$ = 2.3 MΩ. Therefore, the grounded resistor $R_m$ = 50 Ω, marked as ① in Fig. 3, is employed to match the 50 Ω coaxial feed with this high input impedance. Note that the output impedance of our OpAmp design is estimated with the curves in the chip's datasheet to be 145 Ω at the frequency of our interest ~ 414 MHz. To determine the tunable range of the amplification gain with this output impedance, the circuit labeled as ② is then utilized to realize the impedance matching between the estimated 145 Ω output impedance and the 50 Ω measurement port. The circuit ② is composed of a parallel grounded capacitor, $C_m$ = 3.6 pF, and a series inductor, $L_m$ = 27 nH. The circuit labeled as ③ consists of a series resistor $R_f$ = 499 Ω and a grounded adjustable resistor $R_g$. It operates as the negative feedback circuit, and the $R_g$ value can be tuned to regulate the closed-loop gain.

The OpAmp circuit was measured for different values of $R_g$ with an Agilent Technologies N5225A network analyzer. As shown in Fig. 4, the results clearly indicate that by changing the resistor $R_g$ values from 5 Ω to 2000 Ω, the $|S_{21}|$ values of the OpAmp circuit vary from 11.04 to 3.62 dB at 414 MHz, while the $|S_{11}|$ values remain < –10 dB over the entire frequency band, DC to 500 MHz, in all cases. These results confirmed that the OpAmp circuit can realize a tunable closed-loop gain.

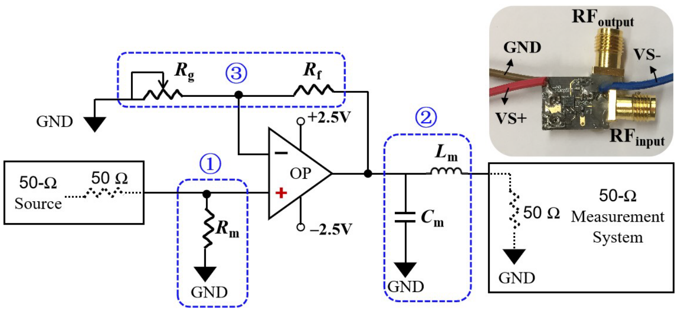


Fig. 3. The diagram of the series-voltage negative feedback amplifier circuit and a photo of the fabricated active OpAmp circuit.

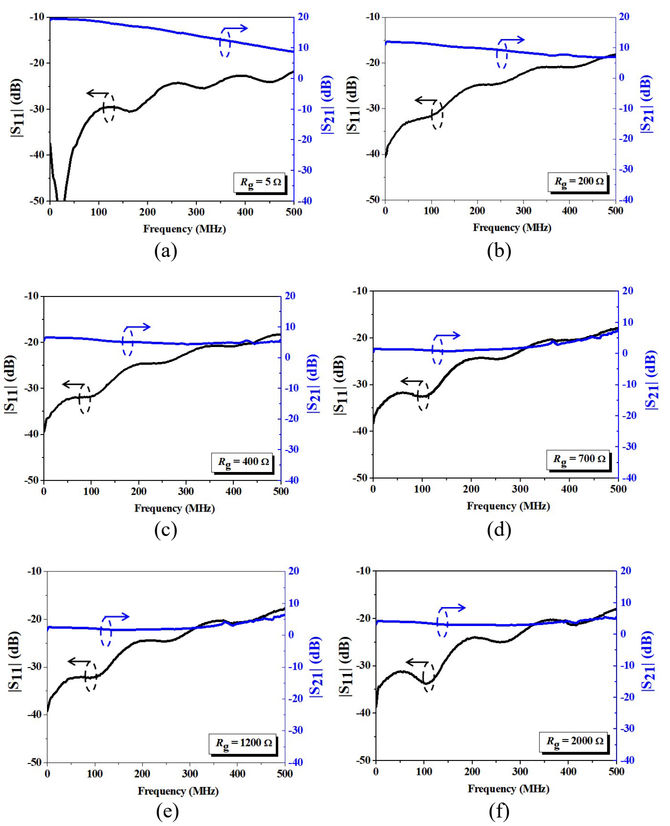


Fig. 4 Measured S-parameter results of the OpAmp circuit for different values of the resistor $R_g$. (a) $R_g$ = 5 Ω. (b) $R_g$ = 200 Ω. (c) $R_g$ = 400 Ω. (d) $R_g$ = 700 Ω. (e) $R_g$ = 1200 Ω. (f) $R_g$ = 2000 Ω.

Second, the passive NFRP ESA illustrated in Fig. 5 was selected as the foundational and reference design [46]. It consists of a coaxial probe-fed rectangular semi-loop driven element and a capacitively loaded rectangular semi-loop. A lumped capacitor is integrated in the center of the top horizontal trace of the NFRP CLL element. It facilitates the desired significant decrease in the electrical size of this radiating element. The capacitor is realized as a 0402 package [51], whose length, width, and height are 1.0 mm, 0.5 mm, and 0.5 mm, respectively.

Moreover, the NFRP ESA design was optimized to directly match it to the output impedance of the OpAmp circuit. Based on the operating characteristics of circuit ② and refined with its measured results, the ESA was co-designed to have a 145 Ω input impedance so that it would be matched to the OpAmp circuit when the driven element is connected to it.

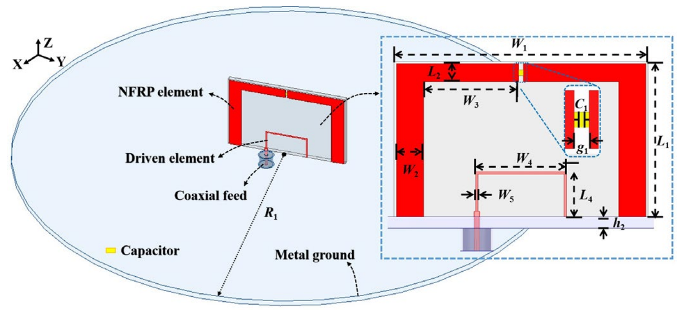


Fig. 5. Passive NFRP ESA configuration. Inset with its design parameters. They are (in millimeters): $L_1$ = 13.6, $L_2$ = 1.6, $L_4$ = 4.0, $W_1$ = 22.4, $W_2$ = 2.7, $W_3$ = 8.1, $W_4$ = 8.0, $W_5$ = 0.2, $g_1$ = 0.4, and $h_2$ = 1.0. The capacitance $C_1$ = 5.6 pF.

Furthermore, this passive NFRP ESA was designed to be extremely electrically small with $ka$ = 0.15. The performance characteristics of this XESA were simulated, and those results are presented in Fig. 6. The $|S_{11}|$ and realized gain values are given in Fig. 6(a) and the input impedance (resistance and reactance) values are given in Fig. 6(b) as functions of the source frequency. It is readily determined that the resonance frequency was $f_0$ = 413.4 MHz and that it has a low peak realized gain value, -1.92 dBi, as anticipated from [52]. The input impedance at $f_0$ is close to 145 Ω, which indicates that the passive XESA is well matched to the OpAmp. Recall that the basic design is a form of the 2D magnetic EZ antenna [46]. As demonstrated in [53], the majority of the currents on the ground plane are confined near to the magnetic EZ radiators. As a consequence, decreasing the radius of the ground plane would have little impact on the impedance matching, but it would cause the peak realized gain to decrease some as the front-to-back ratio (FTBR) value does [53]. The size of the ground plane of the XESA was selected simply for convenience in handling it during the measurement campaign.

Recall that the Chu-Wheeler quality factor corresponding to a $ka$ value is $Q_{\text{Chu}} = (ka)^{-1} + (ka)^{-3}$ [8], [9], which for the passive XESA is $Q_{\text{Chu}}$ = 303. The fundamental bounds on the quality factor, $Q$, of an electric and magnetic antenna are expressed as the lower bounds: $Q_{\text{lb, elec.}} = (3/2) \times \eta_{\text{rad}} \times [(ka)^{-3} \times (ka)^{-1}]$ and $Q_{\text{lb, mag.}} = 2\ Q_{\text{lb, elec.}}$ [8], [54]–[57], where $\eta_{\text{rad}}$ is the antenna's radiation efficiency. The maximum fractional bandwidth ($FBW$) associated with the –3-dB and –10-dB impedance matching points is related to the $Q$ value as $FBW_{3dB} = 2\ /\ Q = 3\ FBW_{10dB}$ [58], [59]. Moreover, the maximum directivity of an electric or a magnetic XESA is $D_{\max}$ = 1.5.

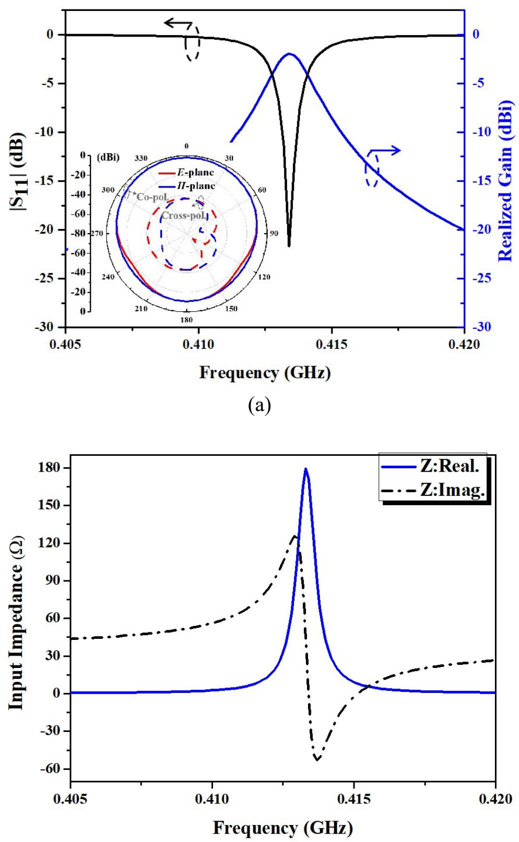


(a)

(b)

Fig. 6. Simulated performance characteristics of the passive NFRP ESA as functions of the source frequency. (a) $|S_{11}|$ and realized gain values with the radiation patterns in the E- and H-planes at the resonance frequency, 413.4 MHz, presented in the insert. (b) Input impedance values.

Recall that the magnetic EZ antennas act as magnetic dipole antennas [46], [60]. The tight upper bound on the ratio of the directivity, $D$, and the quality factor for a passive, lossless, linearly polarized, electrically small magnetic antenna that makes full use of the radian-sphere is [61], [62]:

$$(D / Q_{\text{mag.}})_{\text{max, passive}} \leq (1/2)\,(ka)^3 \qquad (2)$$

The currents on the ground plane associated with the magnetic EZ antennas responsible for impedance matching are basically within the radian-sphere associated with its NFRP element, the main radiator [63]. Also recall that gain of an antenna is the product of its efficiency times its directivity [64]. Consequently, the passive XESA in Fig. 5 has the maximum upper bound on its $GBWP$:

$$(GBWP)_{\text{max, passive}} = D_{\text{max}} \times FBW_{3\text{dB}} \leq (ka)^3 = 3.375\times10^{-3} \qquad (3)$$

With the results shown in Fig. 6(a), one has $FBW_{3\text{dB}} = 3\, FBW_{10\text{dB}} = 3 \times 1.33 \times 10^{-3} = 0.004$. Its peak gain $G_{\text{max}} = -1.92$ dBi $= 0.643$. The simulations further indicate that its radiation efficiency $\eta_{\text{rad}} = 16.25\%$ and its overall efficiency is 16.14% at 413.4 MHz.

Third, the NFRP ESA is integrated with the OpAmp circuit as was demonstrated in Fig. 2. Note that this perpendicular placement of the OpAmp circuit unavoidably makes the operating frequency of the active XESA move to a slightly higher frequency with only a small influence on its impedance matching level, which is easily compensated by optimizing the design parameters of the joint XESA-OpAmp system itself, e.g., the length and the width of the CLL. The parallel placement version, i.e., the OpAmp PCB being parallel to the ESA and separated by a gap, was also considered, but found not to perform as well. There is less coupling between the currents on the OpAmp PCB and those on the CLL and ground plane in the perpendicular version. Furthermore, the impedance matching deteriorates when the parallel version is made more compact (smaller gap) which in turn leads to much lower realized gain values.

The operating mechanisms of the active XESA, i.e., the combined structure, were analyzed by building the corresponding equivalent circuit model based on its physical structure depicted in Fig. 7. Specifically, the rectangular semi-loop driven element was modeled by as a series circuit consisting of four lossy inductors: $L_1$, $L_2$, $L_2$, and $L_1$, together with four resistors, $R_1$, $R_2$, $R_2$, and $R_1$. Similarly, the capacitively-loaded semi-rectangular loop NFRP element is equivalent to a symmetrical series circuit, i.e., inductors $L_3$, $L_4$, and $L_5$ with resistors $R_3$, $R_4$, and $R_5$, and loaded capacitor $C_1$. The radiation resistor of the ESA is represented by the grounded resistor, $R_{\text{rad}}$. Moreover, the capacitive coupling between the driven and NFRP elements is represented by four capacitors $C_2$, $C_3$, $C_3$, and $C_2$. The OpAmp circuit, which consists of the OPA855 chip, matching resistor $R_m$, feedback resistor $R_f$, voltage dividing resistor $R_g$ and circuit loss resistor $R_L$, is connected to the driven element as indicated in Fig. 2. The element values of the optimized equivalent circuit are detailed in Table III.

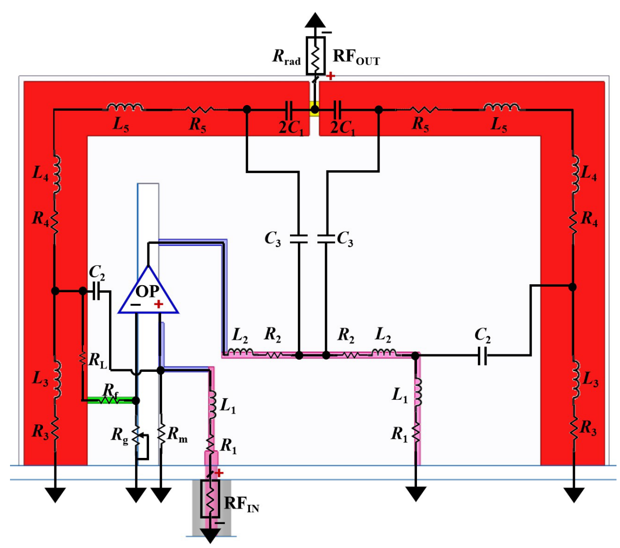


Fig. 7 Equivalent circuit model based on the electromagnetic structure of the active ESA.

TABLE III ELEMENT VALUES OF THE EQUIVALENT CIRCUIT

| | | | | |
|---|---|---|---|---|
| $C_1 = 5.6$pF | $C_2 = 114$pF | $C_3 = 0.6$pF | $L_1 = 2.3$nH | $L_2 = 1.4$nH |
| $L_3 = 0.3$nH | $L_4 = 0.6$nH | $L_5 = 14.8$nH | $R_1 = 0.001\Omega$ | $R_2 = 0.001\Omega$ |
| $R_3 = 0.01\Omega$ | $R_4 = 0.001\Omega$ | $R_5 = 0.001\Omega$ | $R_L = 0.25\Omega$ | $R_m = 50\Omega$ |
| $R_g = \sim2$k$\Omega$ | $R_f = 499\Omega$ | $R_{\text{rad}} = 13.5\Omega$ | *NULL* | |

This circuit model has several series $RLC$ sets in its feedback loop. Therefore, the closed-loop gain of the XESA-OpAmp system follows immediately from (1) as:

$$A_f = 1 + \frac{Z_{eff} + R_f}{R_g} \tag{4}$$

where $Z_{eff}$ is the effective impedance between the resistor $R_f$ and the output port of the OpAmp. Clearly, the presence of $Z_{eff}$ changes the performance of the OpAmp circuit. Moreover, the effective gain of the system becomes proportional to the power radiated, i.e., the power associated with the resistor $R_{rad}$. Therefore, we take the radiation resistor as another port in the equivalent circuit-based co-simulation to obtain the $|S_{21}|$ values to obtain the enhancement of the effective gain of the active ESA. We found this equivalent circuit model attained the desired co-simulation results that guided our active XESA design to be accurate and much more flexible and cost effective in time and effort than any of the commercial software tools available to us.

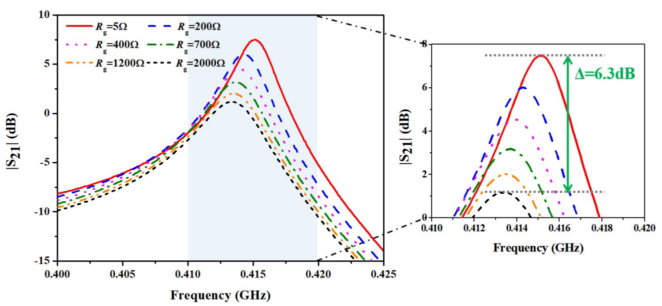


Fig. 8 Simulated $|S_{21}|$ values of the equivalent circuit as functions of the source frequency for six different values of the resistor $R_g$. The insert zooms in on the $|S_{21}| > 0$ dB region.

The equivalent circuit-based co-simulated $|S_{21}|$ values for different $R_g$ values are plotted in Fig. 8. The $|S_{21}| \geq 0$ dB region of these values is shown in the insert. One finds that the $|S_{21}|$ values of the equivalent circuit can be dynamically tuned within a $\Delta = 6.3$ dB range by regulating the resistance of the adjustable resistor $R_g$ from 5 Ω to 2000 Ω. In particular, peak $|S_{21}|$ values of the equivalent circuit model are 7.49, 6.01, 4.53, 3.17, 2.02 and 1.18 dB when $R_g$ is 5, 200, 400, 700, 1200 and 2000 Ω, respectively. The $|S_{21}| \geq 0$ dB values represent potential amplified levels of radiated power facilitated by integrating the XESA into the OpAmp's feedback loop. The equivalent circuit-based co-simulation results confirmed that this combination had a similar tunable closed-loop amplification gain performance as those presented in Fig. 4. Furthermore, when compared with a cascaded design in which the same OpAmp is configured as a simple transmitting amplifier and fed in series to the same ESA which is directly matched to the output impedance of the OpAmp circuit, 145 Ω, our integration approach not only obtains a comparable gain variation range, but it possess several additional merits. These include excellent stability, monotonic gain variation, and trivial frequency variations. Furthermore, simulations of the XESA system with a ground plane whose size is more comparable to the radiator's size show that it also exhibits similar performance characteristics. Consequently, it would be suitable for space-limited systems and would eliminate the transmission line connection losses incurred in any corresponding series version.

## III. Measurement of the Active ESA Prototype

Guided by the equivalent circuit of the combined structure in Fig. 7, the active XESA shown in Fig. 2 was optimized, fabricated, assembled and measured. The components of the fabricated prototype are shown in Figs. 9(a) and 9(b). The S-parameter measurements were carried out using an Agilent Technologies N5225A network analyzer. The far-field characteristics of the prototype, including its effective gain values and corresponding radiation patterns, were measured in an anechoic chamber. The antenna under test (AUT) in the measurement chamber is shown in Fig. 9(c) along with one of the ATTEN TPR3003T-3C DC power supplies which provided the requisite ± 2.5 V to turn on the OpAmp circuit.

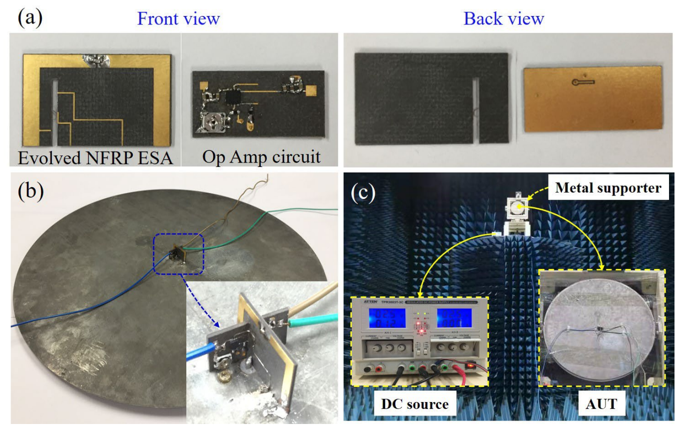


Fig. 9 Fabricated active XESA. (a) Front and back views of each layer before assembly. (b) 3-D isometric view. (c) Antenna under test (AUT) in the chamber.

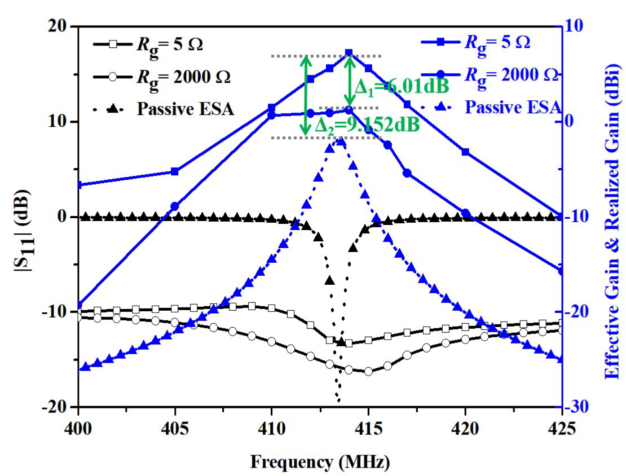


Fig. 10 The simulated $|S_{11}|$ and realized gain values of the passive ESA (dashed lines) and the measured $|S_{11}|$ and effective gain values of the active ESA (solid lines) for several different resistor $R_g$ values.

The S-parameters and the effective gain in the vertical $\theta =$ 0° direction of the developed active XESA, along with its passive counterpart for comparison purposes, are given in Fig.

10. The measured results of the active XESA at the two bounding values of the adjustable resistor $R_g$, i.e., $R_g$ = 5 Ω and 2000 Ω, are presented. Compared with the simulated results of its passive counterpart, the $|S_{11}|$ curves of these two active XESAs (black solid lines) are below –10 dB over the entire set of frequencies shown. This advantageous impedance matching outcome results from the 50 Ω resistor being presented at the positive input port of the OpAmp. Note that both of these curves reach their minimum values near the working frequency of the passive ESA, i.e., near 413.4 MHz.

The measured effective gain curves of the active XESA also exhibit a variation similar to the corresponding circuit model results shown in Fig. 8. We also note that the 3-dB bandwidths of the measured effective gain curves are greatly enlarged. The frequency-dependent amplification associated with the OpAmp circuits compensates for the smaller realized gain values in the neighborhood of the resonance frequency of the passive ESA, thus expanding the bandwidth [65].

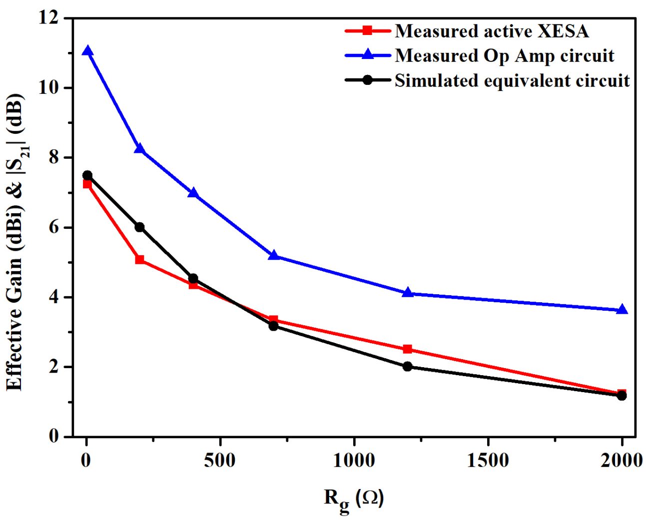


Fig. 11 The measured effective gain values of the active XESA (red solid line), the measured $|S_{21}|$ of the active OpAmp circuit (blue solid line) and the simulated $|S_{21}|$ of the equivalent circuit (black solid line) for the six different resistor $R_g$ values at 414 MHz.

To clearly understand how the $R_g$ value regulates the effective gain, the peak values for different $R_g$ values were extracted from the measured results. These measured results are shown in Fig. 11 (the red line). Specifically, the measured peak effective gain values of the active XESA are 7.232, 5.07, 4.352, 3.339, 2.498 and 1.222 dBi, when $R_g$ = 5, 200, 400, 700, 1200 and 2000 Ω, respectively, at the center frequency, 414 MHz. Its 3-dB gain bandwidth is from 412 to 416 MHz, i.e., $FBW_{3dB}$ = 0.966% with an average gain 5.35 dBi, when $R_g$ is regulated to 5 Ω. Note, in comparison, that a typical passive quarter-wave monopole has $ka$ = 1.57 (10.47 times larger than the XESA) and has a theoretical maximum realized gain of 5.19 dBi [65].

These results clearly demonstrate the adjustability of the effective gain of the active ESA. The prototype achieved a tunable effective gain range from 1.222 - 7.232 dBi when the resistance $R_g$ varied from 5 Ω to 2000 Ω. Hence, the maximum effective isotropic radiated power (*EIRP*), defined as the product of $P_{in}$ and $G_{ant}$ (where $P_{in}$ and $G_{ant}$ are the input power delivered to the antenna and the gain of the antenna, respectively), of the proposed active transmitting XESA witnessed an 8.23 times improvement compared with its passive counterpart [66]. Therefore, the $\Delta_1$ = 6.01 dB variation of the effective gain and the improved *EIRP* for an XESA with $ka$ = 0.15 can meet the requirements of a variety of high-gain, narrow-band transmitting applications in space-constrained and smart platforms.

The *GBWP* of the XESA prototype follows from (3), i.e., it is the product: $GBWP_{measured} = G_{max} \times FBW_{3dB}$. The peak effective gain of the active XESA, 7.232 dBi = 5.287, is $\Delta_2$ = 9.152 dB larger than the realized gain of its passive counterpart. This peak value occurs when $R_g$ = 5 Ω. The corresponding $FBW_{3dB}$ = 0.00966. This means $GBWP_{max,\ measured}$ = 5.287 × 0.0097 = 0.0513. Consequently,

$$GBWP_{active} \,/\, GBWP_{passive,max} = 15.2 \qquad (5)$$

i.e., the measured active XESA had a 15.2 times enhancement of the $GBWP_{max}$ value in comparison to its passive upper bound.

The measured co-polarization and cross-polarization effective gain patterns of the active XESA in its *E*-plane (*yoz*) and its *H*-plane (*xoz*) at the center frequency of it operating band, 414 MHz, for different $R_g$ values are presented in Fig. 12. These patterns are quite similar to those of the passive counterpart displayed in the insert of Fig. 6(a). The peak effective gain value in all of the cases is along the vertical, $\theta$ = 0° direction. The measured cross-polarization levels are 15 dB lower than the co-polarization levels, demonstrating that, like its passive counterpart, the polarization purity of the active XESA is high. In general, the mainlobe of the effective gain patterns in all cases is uniform and stable. Thus, they further demonstrate that the OpAmp circuit has little influence on their shape even though it has a large impact on their peak values. The differences between the backlobes of the passive ESA patterns (in Fig. 6) and those of the measured active XESA (in Fig. 12) are attributed to both simulation and measurement issues. For instance, neither the slender circuit bias lines nor the support structure holding the antenna during its measurements were considered in the simulations. Notably, the large metal support directly behind the antenna that supported it in the test turntable, as shown in Fig. 9, impacted the back-directed fields. Moreover, typical measurement errors added to the discrepancies.

Since we do not have the equipment to directly test the signal-to-noise ratio (SNR) of the transmitting XESA system in our group, the measured noise spectrum on transmission is not available. Nevertheless, we have been able to measure the noise spectrum of the active amplifier circuit as it is turned on and turned off using a Keysight MXA N9030A spectrum analyzer. The measured noise power level that our active XESA prototype witnesses over its ESA's 3-dB gain bandwidth was at most only 2.43 dB. Again, as Fig. 10 demonstrates, the active XESA's measured gain improvement when its prototype was used as a transmitting antenna is 9.152 dB. Because this value is much larger than that of the added noise level, the presence of the latter was not a significant detriment to our active XESA's excellent performance characteristics.

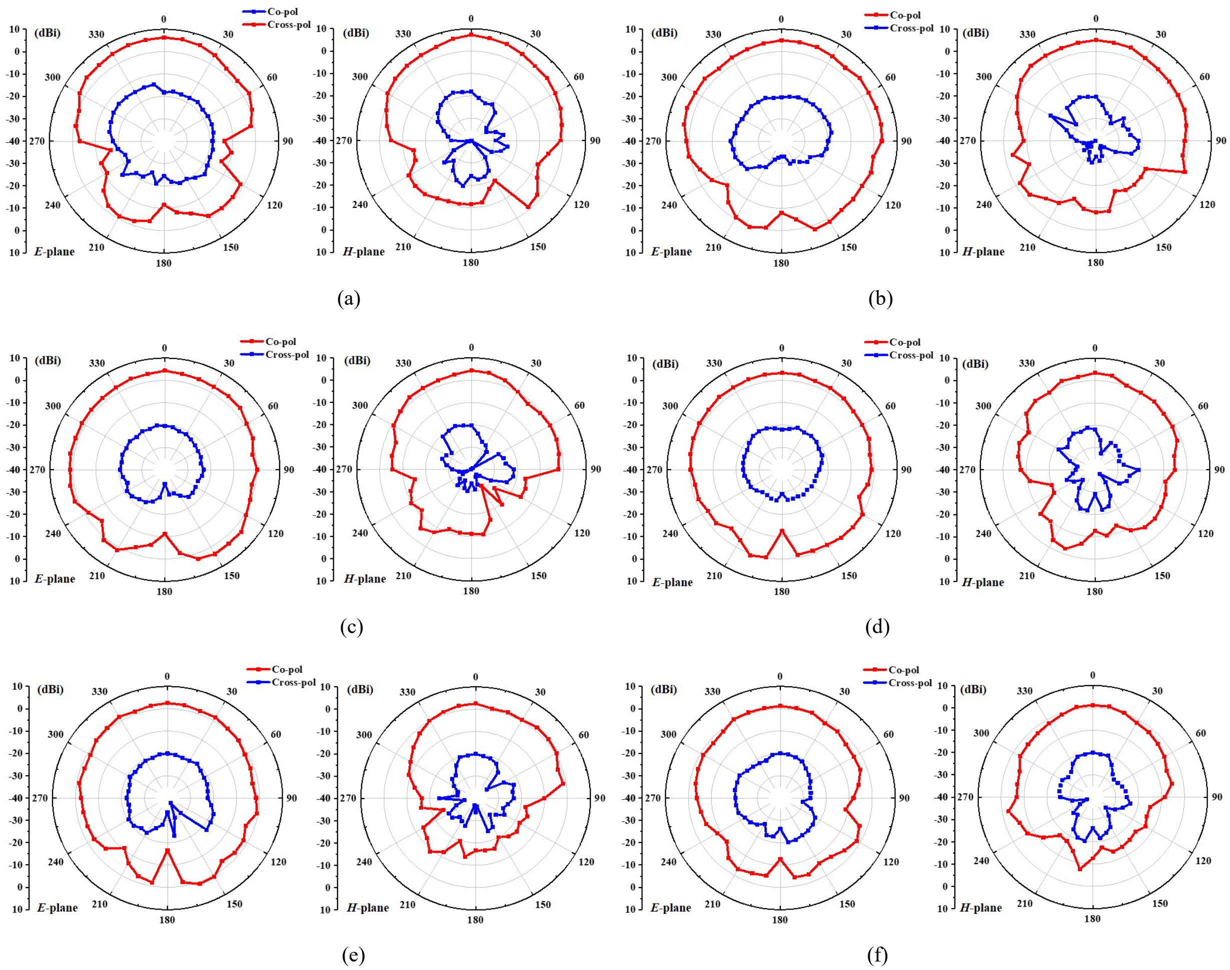


Fig. 12 The measured effective gain patterns of the prototype active ESA operating at 414 MHz for six different values of the variable resistor $R_g$. (a) $R_g = 5\ \Omega$. (b) $R_g = 200\ \Omega$. (c) $R_g = 400\ \Omega$. (d) $R_g = 700\ \Omega$. (e) $R_g = 1200\ \Omega$. (f) $R_g = 2000\ \Omega$.

## IV. Conclusions

An effective-gain-enhanced extremely electrically small NFRP antenna with its *ka* = 0.15 was designed and experimentally demonstrated. The NFRP element of this active XESA was embedded in the negative feedback loop of an OpAmp circuit. Our innovative seamless integration methodology, rather than the standard cascaded configuration, maintained the electrically small size of the system. The measured results, in good agreement with the simulated values of the equivalent circuit, verified its efficacy. The effective gain of the active XESA was significantly larger than the realized gain of its passive counterpart, i.e., 9.152 dBi (8.23 times) larger. Moreover, the effective gain of the systems was demonstrated to be adjustable simply by varying the value of the resistor in the feedback loop. A range of values, from 1.222 to 7.232 dBi, was attained by varying the $R_g$ from 5 to 2000 Ω. The maximum *EIRP* of the active XESA was 8.23 times larger than that of its passive counterpart.

Comparisons between the results of the developed active NFRP XESA and its passive counterpart confirm that it produces an experimentally validated maximum *GBWP* that is 15.2 times larger than its passive upper bound. The polarization purity of the active XESA was high. The effective gain patterns were uniform and stable over its entire bandwidth. Consequently, the advantages of the developed active XESA makes it a potentially viable solution for future space-constrained wireless applications requiring a high effective gain and narrow-band antenna system.

## References

[1] R. W. Ziolkowski and A. Erentok, "Metamaterial-based efficient electrically small antennas," *IEEE Trans. Antennas Propag.*, vol. 54, no. 7, pp. 2113–2130, Jul. 2006.

[2] R. W. Ziolkowski, "An efficient, electrically small antenna designed for VHF and UHF applications," *IEEE Antennas Wireless Propag. Lett.*, vol. 7, pp. 217–220, 2008.

[3] M. -C. Tang, B. Y. Zhou, and R. W. Ziolkowski, "Flexible uniplanar electrically small directive antenna empowered by a modified CPW-feed," *IEEE Antennas Wireless Propag. Lett.*, vol. 15, pp. 914–917, 2016.

[4] J. Choi, F. T. Dagefu, B. M. Sadler, and K. Sarabandi "Electrically small folded dipole antenna for HF and low-VHF bands," *IEEE Antennas Wireless Propag. Lett.*, vol. 15, pp. 718–721, 2016.

[5] S. Lim, J. X. Chen, and C. Cato, "Design of a thin, electrically small, two-element parasitic array with circular polarization," *IEEE Antennas Wireless Propag. Lett.*, vol. 17, pp. 1006–1009, 2018.

[6] H. Bode, *Network Analysis and Feedback Amplifier Design*. New York: Van Nostrand, 1947.

[7] R. M. Fano, "Theoretical limitations on the broadband matching of arbitrary impedances," *J. Franklin Inst.*, vol. 249, pp. 139–154, Feb.1950.

[8] L. J. Chu, "Physical limitations of omni-directional antennas," *J. Appl. Phys.*, vol. 19, no. 12, pp. 1163–1175, 1948.

[9] H. A. Wheeler, "Fundamental limitations of small antennas," *Proc. IRE*, vol. 35, no. 12, pp. 1479–1484, Dec. 1947.

[10] R. F. Harrington, "On the gain and beamwidth of directional antennas," *IRE Trans. Antennas Propag.*, vol. 6, no. 3, pp. 219–225, Jul. 1958.

[11] ——, "Effect of antenna size on gain, bandwidth, and efficiency," *J. Res. Nat. Bur. Stand*, vol. 64, no. 1, pp. 1–12, Jan.-Feb. 1960.

[12] S. E. Sussman-Fort and R. M. Rudish, "Non-Foster impedance matching of electrically-small antennas," *IEEE Trans. Antennas Propag.*, vol. 57, no. 8, pp. 2230–2241, Aug. 2009.

[13] C. R. White, J. S. Colburn, and R. G. Nagele, "A non-Foster VHF monopole antenna," *IEEE Antennas Wireless Propag. Lett.*, vol. 11, pp. 584–587, 2012.

[14] M. Barbuto, A. Monti, F. Bilotti, and A. Toscano, "Design of a non-Foster actively loaded SRR and application in metamaterial-inspired components," *IEEE Trans. Antennas Propag.*, vol. 61, no. 3, 1219–1227, Mar. 2013.

[15] M. M. Jacob and D. F. Sievenpiper, "Gain and noise analysis of non-Foster matched antennas," *IEEE Trans. Antennas Propag.*, vol. 64, no. 12, pp. 4993–5004, Dec. 2016.

[16] F. Albarracín-Vargas, V. Gonzalez-Posadas, F. J. Herraíz-Martinez, and D. Segovia-Vargas, "Design method for actively matched antennas with non-Foster elements," *IEEE Trans. Antennas Propag.*, vol. 64, no. 9, pp. 4118–4123, Sep. 2016.

[17] M. M. Jacob and D. F. Sievenpiper, "Non-Foster matched antennas for high-power applications," *IEEE Trans. Antennas Propag.*, vol. 65, no. 9, pp. 4461–4469, Sep. 2017.

[18] T. -Y. Shih and N. Behdad, "Wideband, non-Foster impedance matching of electrically small transmitting antennas," *IEEE Trans. Antennas Propag.*, vol. 66, no. 11, pp. 5687–5697, Nov. 2018.

[19] P. Jin and R. W. Ziolkowski, "Broadband, efficient, electrically small metamaterial-inspired antennas facilitated by active near-field resonant parasitic elements," *IEEE Trans. Antennas Propag.*, vol. 58, pp. 318-327, Feb. 2010.

[20] N. Zhu and R. W. Ziolkowski, "Broad bandwidth, electrically small antenna augmented with an internal non-Foster element," *IEEE Antennas Wireless Propag. Lett., vol.* 11, pp. 1116-1120, 2012.

[21] ——"Design and measurements of an electrically small, broad bandwidth, non-Foster circuit-augmented protractor antenna," *Appl. Phys. Lett*., vol. 101, 024107, Jul. 2012.

[22] ——"Broad bandwidth, electrically small, non-Foster element-augmented antenna designs, analyses, and measurements," *IEICE Trans. on Commu.*, vol. E96-B, no.10, pp. 2399-2409, Oct. 2013.

[23] M. -C. Tang, N. Zhu and R. W. Ziolkowski, "Augmenting a modified Egyptian axe dipole antenna with non-Foster elements to enlarge its directivity bandwidth," *IEEE Antennas Wireless Propag. Lett.*, vol. 12, pp. 421-424, 2013.

[24] H. Mirzaei and G. V. Eleftheriades, "A resonant printed monopole antenna with an embedded non-Foster matching network," *IEEE Trans. Antennas Propag.*, vol. 61, no. 11, pp. 5363–5371, Nov. 2013.

[25] J. Church, J. -C. S. Chieh, L. Xu, J. D. Rockway, and D. Arceo, "UHF electrically small box cage loop antenna with an embedded non-Foster load," *IEEE Antennas Wireless Propag. Lett.*, vol. 13, pp. 1329–1332, 2014.

[26] M. -C. Tang, T. Shi, and R. W. Ziolkowski, "Electrically small, broadside radiating Huygens source antenna augmented with internal non-Foster elements to increase its bandwidth," *IEEE Antennas Wireless Propag. Lett.*, vol. 16, pp. 712–715, 2017.

[27] T. Shi, M. C. Tang, Z. T. Wu, H. X. Xu, and R. W. Ziolkowski, "Improved signal-to-noise ratio, bandwidth-enhanced electrically small antenna augmented with internal non-Foster elements," *IEEE Trans. Antennas Propag.*, vol. 67, no. 4, pp. 2763–2768, Apr. 2019.

[28] H. Jaafar, D. Lemur, S. Collardey, and A. Sharaiha, "Parametric optimization of a non-Foster circuit embedded in an electrically small antenna for wideband and efficient performance," *IEEE Trans. Antennas Propag.*, vol. 67, no. 6, pp. 3619–3628, Jun. 2019.

[29] S. Lim and H. Ling, "Design of electrically small Yagi antenna," *Electron. Lett.*, vol. 43, no. 5, pp. 3-4, Mar. 2007.

[30] I. T. Nassar, and T. M. Weller, "Development of novel 3-D cube antennas for compact wireless sensor nodes," *IEEE Trans. Antennas Propag.*, vol. 60, no. 2, pp. 1059–1065, Feb. 2012.

[31] Y. -H. Yu, Z. -Y. Zong, W. Wu, and D. -G. Fang, "Dielectric slab superstrate electrically small antennas with high gain and wide band," *IEEE Antennas Wireless Propag. Lett.*, vol. 19, no. 9, pp. 1476–1480, Sept. 2020.

[32] P. Jin, and R. W. Ziolkowski, "High-directivity, electrically small, low-profile near-field resonant parasitic antennas," *IEEE Antennas Wireless Propag. Lett.*, vol. 11, pp. 305–309, 2012.

[33] M. -C. Tang, B. Zhou, Y. Duan, X. Chen, and R.W. Ziolkowski, "Pattern-reconfigurable, flexible, wideband, directive, electrically small near-field resonant parasitic antenna," *IEEE Trans. Antennas Propag.*, vol. 66, no. 5, pp. 2271-2280, May 2018.

[34] P. Jin and R. W. Ziolkowski, "Metamaterial-inspired, electrically small, Huygens sources," *IEEE Antennas Wireless Propag. Lett.*, vol. 9, pp. 501-505, May 2010.

[35] R. W. Ziolkowski, "Low profile, broadside radiating, electrically small Huygens source antennas," *IEEE Access*, vol. 3, pp. 2644-2651, Dec. 2015.

[36] M. -C. Tang, Z. Wu, T. Shi, H. Zeng, W. Lin, and R. W. Ziolkowski, "Dual-linearly polarized, electrically small, low-profile, broadside radiating, huygens dipole antenna, *IEEE Trans. Antennas Propag.*, vol. 66, no. 8, pp. 3877-3885, Aug. 2018.

[37] W. Lin and R. W. Ziolkowski, "Electrically-small, low-profile, Huygens circularly polarized antenna," *IEEE Trans. Antennas Propag.*, vol. 66, no. 2, pp. 636-643, Feb. 2018.

[38] K. V. Caekenberghe, N. Behdad, K. M. Brakora, and K. Sarabandi, "A 2.45-GHz electrically small slot antenna," *IEEE Antennas Wireless Propag. Lett.*, vol. 7, pp. 346–348, 2008.

[39] L. Salman, S. Salman, S. Jahangirian, M. Abraham, F. German, C. Blair, and P. Krenz, "Energy efficient IoT-based smart home," *IEEE 3$^{rd}$ World Forum on Internet of Things (WF-IoT)*, pp. 526–529, 2016.

[40] C. S. Abella, S. Bonina, A. Cucuccio, S. D. Angelo, G. Giustolisi, A. D. Grasso, A. Imbruglia, G. S. Mauro, G. A. M. Nastasi, G. Palumbo, S. Pennisi, G. Sorbello, and A. Scuderi "Autonomous energy-efficient wireless sensor network platform for home/office automation," *IEEE Sens. J.*, vol. 19, no. 9, pp. 3501–3512, May. 2019.

[41] A. Dierck, H. Rogier, and F. Declercq, "A wearable active antenna for global positioning system and satellite phone," *IEEE Trans. Antennas Propag.*, vol. 61, no. 2, pp. 532–538, Feb. 2010.

[42] K. Cho and S. Hong, "Design of a VHF/UHF/L-band low-power active antenna for mobile handsets", *IEEE Antennas Wireless Propag. Lett.*, vol. 11, pp. 45–48, 2012.

[43] W. T. Khan, A. L. Vera López, A. Ç. Ulusoy, and J. Papapolymerou, "Packaging a W-band integrated module with an optimized flip-chip interconnect on an organic substrate," *IEEE Trans. Microw. Theory Techn.*, vol. 62, no. 1, pp. 64–72, Jan. 2014.

[44] N. Hasegawa, and N. Shinohara, "C-band active-antenna design for effective integration with a GaN amplifier," *IEEE Trans. Microw. Theory Techn.*, vol. 65, no. 12, pp. 4976–4983, Dec. 2017.

[45] Y. X. Song, Y. Q. Wu, J. Yang, Y. Tian, W. Tong, Y. J. Chen, C. T. Wang, X. H. Tang, J. Benedikt, and K. Kang, "A compact Ka-band active integrated antenna with a GaAs amplifier in a ceramic package," *IEEE Antennas Wireless Propag. Lett.*, vol. 16, pp. 2416–2419, 2017.

[46] A. Erentok, and R. W. Ziolkowski, "Metamaterial-inspired efficient electrically small antennas," *IEEE Trans. Antennas Propag.*, vol. 56, no. 3, pp. 691–707, Mar. 2008.

[47] Datasheet for OPA855. Dallas, Texas 75265, U.S.A.: Texas Instruments Inc., 2018.

[48] W. Jung, *OpAmp Applications Handbook*, Burlington, MA: Elsevier, 2005.

[49] A. J. Simmons and D. G. Bodnar, "Gain of active antenna systems: Antenna standards committee requests input," *IEEE Antennas Propag. Soc. Newslett.*, vol. 31, no. 5, p. 62, Oct. 1989.

[50] D. Segovia-Vargas, D. Castro-Galán, L. E. García-Muñoz, and G. Posadas, "Broadband active receiving patch with resistive equalization," *IEEE Trans. Microw. Theory Techn.*, vol. 56, no. 1, pp. 56–64, Jan. 2008.

[51] Datasheet for 0402CG5R6C500NT, Zhaoqing, Guangdong, China: Fenghua Advanced Technology Inc., 2016.

[52] C. Lin, R. W. Ziolkowski, J. A. Nielsen, M. H. Tanielian, and C. L. Holloway, "An efficient, low profile, electrically small, three-dimensional, very high frequency magnetic EZ antenna," *Appl. Phys. Lett.*, vol. 96, no. 10, Feb. 2010.

[53] R. W. Ziolkowski, "The directivity of a compact antenna: An unforgettable figure of merit*," EPJ Appl. Metamat.*, vol. 4, 7, 2017.

[54] J. S. McLean, "A re-examination of the fundamental limits on the radiation Q of electrically small antennas," IEEE Trans. Antennas

Propag., vol. 44, no. 5, pp. 672–676, May 1996.
[55] H. L. Thal, “New radiation Q limits for spherical wire antennas,” *IEEE Trans. Antennas Propag.*, vol. 54, no. 10, pp. 2757-2763, Oct. 2006.
[56] S. R. Best, “A low Q small linear and elliptical polarized spherical dipole antennas,” *IEEE Trans. Antennas Propag.*, vol. 53, no. 3, pp. 1047–1053, Mar. 2005.
[57] ——, “A low Q electrically small magnetic (TE mode) dipole,” *IEEE Antennas Wireless Propag. Lett.*, vol. 8, pp. 572–575, 2009.
[58] A. D. Yaghjian and S. R. Best, “Impedance, bandwidth, and Q of antennas,” *IEEE Trans. Antennas Propag*., vol. 53, no. 4, pp. 1298-1324, 2003.
[59] R. W. Ziolkowski, M. -C. Tang, and N. Zhu, “An efficient, broad bandwidth, high directivity, electrically small antenna,” *Microw. Opt. Technol. Lett.*, vol. 55, no. 6, pp. 1430–1434, Jun. 2013.
[60] R. W. Ziolkowski, P. Jin and C. -C. Lin, “Metamaterial-inspired engineering of antennas,” *Proc. IEEE*, vol. 99, pp. 1720-1731, Oct. 2011.
[61] M. Gustafsson, C. Sohl, and G. Kristensson, “Physical limitations on antennas of arbitrary shape,” *Proc. R. Soc. A*, vol. 463, pp. 2589–2607, 2007.
[62] ——, “Illustrations of new physical bounds on linearly polarized antennas,” *IEEE Trans. Antennas Propag.*, vol. 57, no. 5, pp. 1319-1327, 2009.
[63] R. W. Ziolkowski, “The directivity of a compact antenna: An unforgettable figure of merit,” *EPJ Appl. Metamat.*, vol. 4, 7, 2017.
[64] C. A. Balanis, *Antenna Theory Analysis and Design*, 3rd Edition, Hoboken: John Wiley & Sons, 2005.
[65] T. Macnamara, *Introduction to Antenna Placement and Installation*. Chichester, UK: John Wiley and Sons, 2010.
[66] N. Hasegawa, and N. Shinohara, “C-band active-antenna design for effective integration with a GaN amplifier,” *IEEE Trans. Microw. Theory Techn.*, vol. 65, no. 12, pp. 4976–4983, Dec. 2017.

**Yaqing Yu** (S’19) received the B.S. degree in electronic science and technology in the School of Physics and Electronic-electrical Engineering, Ningxia University (NXU), Ningxia, China, in 2017. She is currently pursuing the Ph. D degree in circuits and systems in the School of Microelectronics Communication Engineering, Chongqing University, Chongqing, China.

Her research interests include active antenna and filter designs, and their applications.

**Ming-Chun Tang** (S’12–M’13–SM’16) received the B. S. degree in physics from the Neijiang Normal University, Neijiang, China, in 2005 and the Ph. D. degree in radio physics from the University of Electronic Science and Technology of China (UESTC), in 2013. From August 2011 to August 2012, he was also with the Department of Electrical and Computer Engineering, The University of Arizona, Tucson, AZ, USA, as a Visiting Scholar. He is currently a full Professor in the School of Microelectronics and Communication Engineering, Chongqing University, China. His research interests include electrically small antennas, RF circuits, metamaterial designs and their applications.

Prof. Tang was a recipient of the National Science Fund for Excellent Young Scholars in 2019. He is the founding Chair of the IEEE AP-S / MTT-S Joint Chongqing Chapter. He has also served on the review boards of various technical journals, and many international conferences as a General Chair, TPC Member, Session Organizer, and the Session Chair.

**Da Yi** (S’15 – M’ 19) received the B. S. degree and Ph. D. degree in electronic science and technology from Zhejiang University in 2014 and 2019, respectively. He currently works in Chongqing University, Chongqing, China as a tenure-track assistant professor.

Dr. Yi was the recipient of the awards in several international conferences, including Best Student Paper award in IWS 2016 and EMC COMPO 2019, Best Paper award in ISEMC 2019, and the Young Investigator Training Program (YITP) award in SPI 2017. His current research interest is the interference decoupling and noise suppression in antenna arrays and high-speed circuits.

**Dingmou Hong** (S’19) received the B.S. degree in communication engineering in the School of College of Information Science and Engineering, Guilin University of Technology (GUT), Guilin, China, in 2019. He is currently pursuing the M. S. degree in electronic science and technology in the School of Microelectronics Communication Engineering, Chongqing University, Chongqing, China.

His current research interests include helix antenna and high gain antenna designs, and their applications.

**Ting Shi** (S’16 – M’ 20) received the B.S. degree in electronic information science and technology from University of Electronic Science and Technology of China (UESTC), Chengdu, China, in 2014, and the M.S. and PhD. degree in circuit and system from Chongqing University, Chongqing, China, in 2017 and 2020, respectively. In Sep. 2018–Sep. 2019, she was also with the Department of Electrical and Computer Engineering, National University of Singapore (NUS), Singapore, as a Visiting Graduate.

She is currently a Post-Doctoral Fellow in the School of Electronic Science and Engineering (National Exemplary School of Microelectronics), UESTC, Chengdu, China. Her research interests include microwave antenna and array and metasurfaces absorber. Dr. Shi was a recipient of the Student Paper Award in the IEEE 7th Asia-Pacific Conference on Antennas and Propagation (2017 APCAP) and the Newcomer Award for Graduate Candidates in 2019 the 1st China Meta Materials Conference.

**Richard W. Ziolkowski** (M’87–SM’91–F’94-LF’20) received the B. Sc. (magna cum laude) degree (Hons.) in physics from Brown University, Providence, RI, USA, in 1974; the M.S. and Ph.D. degrees in physics from the University of Illinois at Urbana-Champaign, Urbana, IL, USA, in 1975 and 1980, respectively; and an Honorary Doctorate degree from the Technical University of Denmark, Kongens Lyngby, Denmark in 2012.

He is currently a Distinguished Professor in the Global Big Data Technologies Centre in the Faculty of Engineering and Information Technologies (FEIT) at the University of Technology Sydney, Ultimo NSW Australia. He became a Professor Emeritus at the University of Arizona in 2018, where he was a Litton Industries John M. Leonis Distinguished Professor in the Department of Electrical and Computer Engineering in the College of Engineering and was also a Professor in the College of Optical Sciences. He was the Computational Electronics and Electromagnetics Thrust Area Leader with the Engineering Research Division of the Lawrence Livermore National Laboratory before joining The University of Arizona, Tucson, AZ, USA, in 1990. His current research interests include the application of new mathematical and numerical methods to linear and nonlinear problems dealing with the interaction of electromagnetic and acoustic waves with complex linear and nonlinear media, as well as metamaterials, metamaterial-inspired structures, nano-structures, and other classical and quantum applications-specific configurations.

Prof. Ziolkowski was the recipient of the 2019 IEEE Electromagnetics Award (IEEE Technical Field Award). He became a Fellow of Optica (previously the Optical Society of America, OSA) in 2006 and the American Physical Society (APS) in 2016. He was the 2014-2015 Australian DSTO Fulbright Distinguished Chair in Advanced Science and Technology. He served as the President of the IEEE Antennas and Propagation Society (AP-S) in 2005 and has had many other AP-S leadership roles. He is also actively involved with the International Union of Radio Science (URSI), the European Association on Antennas and Propagation (EurAAP), and the International Society for Optics and Photonics (SPIE) professional societies.